European Space Agency

ADVANCED CLOUDS, AEROSOLS AND WATER VAPOUR PRODUCTS FOR SENTINEL-3/OLCI

Retrieval of Total Column Water Vapor from MERIS/OLCI and MODIS above Land- and Ocean Surfaces

Algorithm Theoretical Basis Document (ATBD)

and

Input/Output Data Definition (IODD)

Issue 1.1, 20.10.2015

ESRIN/Contract No: 4000111860/14/I-NB

prepared by

Rene Preusker, Hannes Diedrich, Jürgen Fischer

Document, Version	Date	Changes	Originator
ATBD, v1.0_draft	20.01.2015	Original	Jürgen Fischer, Rene Preusker, Hannes Diedrich
ATBD v1.0	22.07.2015	Original	Jürgen Fischer, Rene Preusker
ATBD v1.1	10.10.2015	Minor changes	Jürgen Fischer, Rene Preusker

Table of Content

Acronyms and Abbreviations

AATSR	Advanced Along Track Scanning Radiometer
AERONET	AErosol RObotic NETwork
AOD	Aerosol Optical Depth
ANN	Artificial neural network
ATBD	Algorithm Theoretical Basis Document
BC	Brockmann Consult
BEAM	Basic Envisat Tool for AATSR & MERIS (http://envisat.esa.int /services/beam/)
CNES	Centre National d'Etudes Spatiales
CTP	Cloud-top pressure
DJF	Design justification file
DPM	Detailed Processing Model
DQWG	Data quality working group
DUE	ESA Data User Element programme (http://due.esrin.esa.int/)
ECSS	European Co-operation for Space Standardisation (documents available at ESTEC at the Requirements and Standards Division)
Envisat	ESA satellite (see http://envisat.esa.int/)
EO	Earth Observation
ESA	European Space Agency (http://www.esa.it/export/esaCP/index.html)
ESTEC	European Space Research and Technology Centre
ESRIN	European Space Research Institute (http://www.esa.it/export/esaCP/index)
FUB	Freie Universität Berlin
FoV	Field of View
GCOS	Global Climate Observing System
GEWEX	Global Energy and Water Exchanges Project
GPS	Global Positioning System
GUAN	GCOS Upper Air Network
GVaP	GEWEX Global Water Vapor Project
HITRAN	High-resolution transmission molecular absorption database
HOAPS	Hamburg Ocean Atmosphere Parameters and Fluxes from Satellite
ICAP	International Cooperative for Aerosol Prediction (ICAP)
IODD	Input Output Data Definition Doc.
ISCCP	GEWEX International Satellite Cloud Climatology Project
L1/L2	Level 1 / Level 2
LBL	Line-by-line
LUT	Look-up table
MERIS	Medium Resolution Imaging Spectrometer Instrument (http://envisat.esa.int/)
MODIS	Moderate Resolution Imaging Spectroradiometer (on board the NASA EOS-Aqua satellite)
MOMO	Matrix Operator Modell
MSG	METEOSAT Second Generation
MWR	Microwave Radiometer
NASA	National Aeronautics and Space Administration
OE	Optimal estimation
OLCI	Ocean and Land Colour Instrument on board Sentinel-3
PARASOL	Polarization & Anisotropy of Reflectances for Atmospheric Sciences mission
PDF	Portable Document Format
POLDER	Polarization and Directionality of the Earth's Reflectances
PVR	Product Validation and evolution Report
QA4EO	Quality Assurance framework for Earth Observation
RB	Requirements baseline
RTC / RTM	Radiative Transfer Code / Model
RR	Reduced Resolution
SCIAMACHY	Scanning Imaging Absorption Spectrometer for Atmospheric Cartography
SEOM	ESA Scientific Exploitation of Operational Missions Element programme (http:// seom.esa.int/)
SOS	Successive Order of Scattering
SoW	Statement of Work
TCWV	Total Column Water Vapour
TOA	Top of atmosphere
VISAT	Visualisation and analysis tool

References

Applicable Documents

[AD-1]	EOP-GMQ, 2014: *SEOM S3-CAWA: advanced Clouds, Aerosols and WAter vapour products for Sentinel-3/OLCI, Statement of Work*. GMES-GSEG-EOPG-SW-13-0047, iss. 1 rev0, dated 14.01.2014 (https://earth.esa.int/web/sppa/activities/cawa/projects-documents/)
[AD-2]	Fox, N. et al., 2010: *A guide to establishing validated models, algorithms and software to underpin the Quality Assurance requirements of GEO* (http://www.qa4eo.org/docs/QA4EO-QAEO-GEN-DQK-002_v4.0.pdf)
[AD-3]	Eaton et al. , 2011: *NetCDF Climate and Forecast (CF) Metadata Convention* (http://cf-pcmdi.llnl.gov/)
[AD-4]	Fischer, J. et al. 2015: *CAWA – Requirement Baseline Document* (https://earth.esa.int/web/sppa/activities/cawa/projects-documents/)

Reference Documents

[RD-1]	DUE GlobVapour - Algorithm Theoretical Basis Document L2 MERIS, Version 3.0 (http://www.globvapour.info/download/GlobVapour_D16_ATBD_L2_MERIS_v3.0.pdf)
[RD-2]	DUE GlobVapour – Product Validation Report, Cross-Comparison, Version 1.1 (http://www.globvapour.info/download/GlobVapour_D19_PVR_CrossComp_V1.1.pdf)
[RD-3]	Hollmann et al. (2013) The ESA Climate Change Initiative: Satellite Data Records for Essential Climate Variables ESA Climate Change Initiative. Bull. Amer. Meteor. Soc., 94, 1541–1552.
[RD-4]	GCOS, 2010: Implementation Plan for the Global Observing System for Climate in Support of the UNFCCC (2010 update, November 2009).
[RD-5]	GCOS, 2011: Systematic observation requirements for satellite-based data produced for climate, 2011 updates. GCOS -154 Global Climate Observing System, 2011. http://www.wmo.int/pages/prog/gcos/Publications/gcos-154.pdf

1 Introduction

1.1 Purpose

This document provides information about the physical background, technical structure and the functional principle of the CAWA total column water vapour retrieval as defined within the SEOM 'Advanced Clouds, Aerosols and WAter vapour products for Sentinel-3/OLCI' CAWA project, which aims to the development and improvement of advanced atmospheric retrieval algorithms for the Envisat/MERIS and Sentinel-3/OLCI mission.

1.2 Structure of the document

This document addresses the *Algorithm Theoretical Baseline* (ATBD) and the *Input/Output Data Definition* (IODD). It is structured as following:

- Overview of the retrieval algorithm scheme (Chapter 2)
- Description of the forward operator (Chapter 3)
- Assumptions and limitations (Chapter 4)
- Conclusions (Chapter 5).

1.3 Satellite instruments

The measurements of the satellite sensors MERIS, MODIS and OLCI used in this study are briefly described in the following.

1.3.1 MERIS and OLCI

The key mission objective for the Sentinel-3 OLCI instrument is the continuity of the ENVISAT MERIS instrument capability. The primary mission of OLCI is the observation of the spectral distribution of upwelling radiance just above the sea surface (the water-leaving radiance) that is then used to estimate a number of geophysical parameters through the application of specific bio-optical algorithms. Atmospheric correction for ocean colour data is challenging (International Ocean Colour Coordinating Group - IOCCG, 2010) as only about 4% of the radiation measured by a satellite instrument originates from the water surface and sensors require high signal to noise ratio (SNR), particularly for the 'blue' bands (Donlon et al, 2012). This requires an accurate retrieval and description of the atmospheric state with respect to scattering and absorption processes. This points to the secondary objective, the detection of atmospheric properties, which include cloud detection (pixel classification) and aerosol detection, which is important not only for atmospheric correction but also for the monitoring of air-pollution.

The S-3 OLCI instrument is based on the opto-mechanical and imaging design of ENVISAT MERIS (see Table 1). The instrument is a quasi-autonomous, self contained, visible push-broom imaging spectrometer and incorporates the following significant improvements when compared to MERIS:

- An increase in the number of spectral bands (from 15 to 21),
- Improved SNR and a 14-bit analogue to digital converter,
- Improved long-term radiometric stability,
- Mitigation of sun-glint contamination by tilting cameras in westerly direction by 12.6°,
- Complete coverage over both land and ocean at 300 m Full-Resolution (FR),
- Improved instrument characterization including stray-light, camera overlap, and calibration diffusers.

The cameras are arranged to slightly overlap with each other to cover a wide 68.5° across-track field of view as shown in Figure 1. The OLCI swath is not centred at nadir (as in the MERIS design) but is

tilted 12.6° westwards to mitigate the negative impact of sun-glint contamination that affects almost half of the MERIS observations at sub-tropical latitudes.

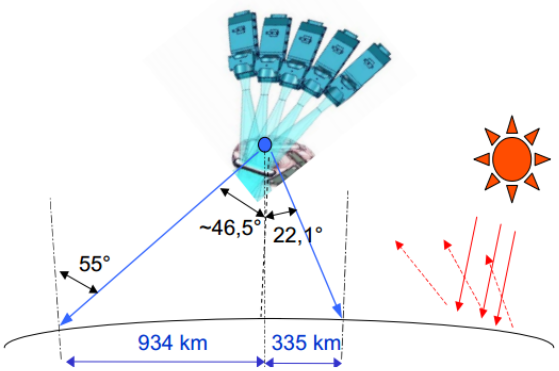

Figure 1: OLCI features a tilted field of view to avoid sun-glint.

OLCI bands are optimised to measure ocean colour over the open ocean and coastal zones. A new channel at 1.02 µm has been included to improve atmospheric and aerosol correction capabilities, additional channels in the O_2 A-band spectral region are included for improved cloud top pressure (height) and water vapour retrieval, and a channel at 673 nm has been added for improved chlorophyll fluorescence measurements. In principle, the OLCI programmable acquisition design allows spectral bands to be redefined in both location and width during commissioning of the instrument after which time they will be fixed for the mission duration.

Table 1: The spectral bands of OLCI and MERIS.

OLCI Band	Center [nm]	Width [nm]
Oa1	400	15
Oa2	412,5	10
Oa3	442,5	10
Oa4	490	10
Oa5	510	10
Oa6	560	10
Oa7	620	10
Oa8	665	10
Oa9	673,75	7,5
Oa10	681,25	7,5
Oa11	708,75	10
Oa12	753,75	7,5
Oa13	761,25	2,5
Oa14	764,375	3,75
Oa15	767,5	2,5
Oa16	778,75	15
Oa17	865	20
Oa18	885	10
Oa19	900	10
Oa20	940	20
Oa21	1020	40

MERIS Band	Center [nm]	Width [nm]
Me1	412,5	10
Me2	442,5	10
Me3	490	10
Me4	510	10
Me5	560	10
Me6	620	50
Me7	670	15
Me8	681,25	10
Me9	708,75	10
Me10	753,75	10
Me11	761,875	3,75
Me12	778,75	15
Me13	865	10
Me14	885	10
Me15	900	10

For the water vapour retrieval the MERIS channels Me14 and Me15 are used as reference and the absorption band, resp.. For OLCI there are two reference channels, Oa18 and Oa21, and two absorption channels Oa19 and Oa20 (see Table 1).

1.3.2 MODIS

The EOS MODIS instrument provides high radiometric sensitivity (12 bit) in 36 spectral bands ranging in wavelength from 0.4 µm to 14.4 µm. The responses are custom tailored to the individual needs of the user community and provide exceptionally low out-of-band response. Two bands are imaged at a nominal resolution of 250 m at nadir, with five bands at 500 m, and the remaining 29 bands at 1 km. A ±55-degree scanning pattern at the EOS orbit of 705 km achieves a 2,330-km swath and provides global coverage every one to two days. For more details of the MODIS instrument and its applications see http://modis.gsfc.nasa.gov/about/design.php. The MODIS instrument is flying on board the Terra (10:30 equator crossing time) and on board Aqua (13:30 equator crossing time). The later is also part of the A-train.

Table 2: The spectral bands of MODIS within the solar spectral domain, the spatial resolution is 250 m for Md1-Md2 (dark grey), 500m for Md3-Md7 (light grey) and 1000m for Md8-Md19.

MODIS Band	Center [nm]	Width [nm]
Md1	645	50
Md2	858,5	35
Md3	469	20
Md4	555	20
Md5	1240	20
Md6	1640	24
Md7	2130	50
Md8	412,5	15
Md9	443	10
Md10	488	10
Md11	531	10
Md12	551	10
Md13	667	10
Md14	678	10
Md15	748	10
Md16	869,5	15
Md17	905	30
Md18	936	10
Md19	940	50

Given the wide swath of the MODIS instrument, which stretches over 2330km, the tilted swath of OLCI can be simulated. This will provide an accurate assessment whether any problems with the surface elevation are to be expected and whether an ortho-rectification would be required. Reducing the swath will also improve the agreement of the coverage characteristics with OLCI, including the revisit rates, yet not fully given the different orbital heights of 814.5 km and 705 km for Sentinel-3 and EOS-Aqua respectively. In terms of the spatial resolution, only the OLCI Reduced Resolution products can be generated. MODIS only offers a 250 m resolution for the first two bands, Md1 and Md2. Md3-Md7 features 500 m, while the remaining ones feature 1000 m (see Table 2).

For the water vapour retrieval the MODIS channels Md2 and Md5 (averaged over 4 b4 pixels) are used as reference and the three channels Md17 to Md19 for the water vapour absorption.

2 Water Vapour Algorithm - Overview

The retrieval detects total column water vapor (TCWV) over cloud-free water- and land surfaces. The algorithm is based on differential absorption using satellite measurements within the $\rho\sigma\tau$-H_2O absorption band between 890 and 1000 nm ([Fischer, 1988], [Gao et al, 1990], [Bartsch et al, 1996], [Albert et al, 2001], [Albert et al, 2005]). The procedure can be adapted easily for different sensors,

which measure reflected sunlight in this spectral region. It requires measurements in at least one absorption band and one nearby band with only little or no absorption (reference bands). It has been initially designed for the Medium Resolution Imaging Spectrometer MERIS ([Fischer, 1988],[Lindstrot et al, 2012]) and has been recently adapted for the Moderate Resolution Imaging Spectroradiometer (MODIS) [Diedrich et al, 2014] and the Ocean- and Land Color Instrument (OLCI).

Measured radiances from satellites in a water vapor absorption band carry information about the TCWV. The backbone of the retrieval is the forward operator that simulates TOA radiances. A 1D-Var scheme optimizes the difference between simulated and measured radiances band by iteratively varying the TCWV value. Thereby, information from each absorption band is used, following the scheme after Rodgers (2000) (see Sect. 3.3.1).

For the forward operator, radiative transfer simulations (RTS) were performed for various atmospheric conditions and stored in look up tables (LUTs). The gaseous absorption coefficients, based on HITRAN 2012 [Rothman et al, 2013] data were calculated using an advanced k-distribution routine for different standard temperature profiles ([Bennartz and Fischer, 2000], [Doppler et al, 2014]). The temperature profile is chosen depending on the surface temperature, which is taken from reanalysis data such as ERA-interim. Interactions with aerosol particles and molecules are simulated with the radiative transfer model MOMO [Hollstein and Fischer, 2012] (see Sect. 3.2).

In the forward operator, the atmospheric transmittance is modelled by transmittance due to gaseous absorption (mainly water vapour) and multiplied by a scattering correction. This parameterisation decreases the number of dimensions of the LUTs and thus computation time. Additionally, it enables an easy structure of the forward operator concerning the difference between water- and land surfaces. Here, only the determination of the scattering correction is different.

The algorithm does not rely on prior knowledge and background information. Nevertheless, estimates of AOT, and/or the surface temperature from ERA-interim are beneficial. Uncertainty estimates are provided by taking into account all relevant sources of error such as sensor noise, and errors of forward modelling parameters such as AOT, aerosol vertical distribution, surface reflectance, surface elevation and temperature.

The adaption to new sensors is easily achievable because only the LUTs for transmittance forward operator have to be simulated for the specific band setup. The RTSs for the scattering factor are already performed in 1 nm steps for the wavelength range between 800 and 1300 nm. From that the LUTs for f and the surface reflectance can easily be adapted for the new band setup.

3 Algorithm description

3.1 Theoretical description

Water vapour has various absorption features in the solar and terrestrial spectrum, which is due to a combination of the three fundamental vibration modes of the water molecule. Measurements of reflected sunlight in this absorption bands enables a determination of TCWV provided that the following conditions are given:

1. Solar radiation is available, limiting the retrieval to daytime measurements
2. The band used is located in a sufficient sensitive part of the spectrum, and is not saturated.
3. The surface albedo is sufficiently bright and can be accurately estimated, precluding dark ocean surfaces.
4. The photon paths through the atmosphere and the reflection function of the surface are known.
5. The lower troposphere, holding the main part of the TCWV, is not masked by clouds or optical thick aerosol layers.

The NIR spectral range is perfectly suited for daytime, cloud-free retrieval of TCWV over land. Here, almost all surfaces provide a good background. The retrieval is based on the differential absorption technique ([Fischer, 1988], Gao et al, [1993], [Lindstrot et al, 2012]). The basic principle of the method is the comparison of the measured radiance in an absorption band to a close by band with no or few absorption features.

The radiance on the top of atmosphere (TOA) $L_{TOA}(\lambda)$ at a certain wavelength or band can be approximated by:

$$L_{TOA}(\lambda) = E_0(\lambda)\ \alpha(\lambda)\ T(\lambda)\cos(\theta_s) / \pi / (1-H(\lambda)\,\alpha(\lambda)) + L_{path}(\lambda) \quad (1)$$

where λ is the wavelength, $E_0(\lambda)$ the solar flux (solar constant at the wavelength), $T(\lambda)$ the total atmospheric transmittance, $\alpha(\lambda)$ the surface reflectance, θ_s the solar zenith angle, $L_{path}(\lambda)$ is the path scattered radiance and $H(\lambda)$ the hemispheric reflectance.

For monochromatic radiation, neglecting scattering processes along the photon path, the transmittance T through the atmosphere can be related to its optical depth τ and the air mass $\mu=1/cos(\theta_s)$, following the Beer-Lambert law:

$$T = exp(\tau/\mu) \quad (2)$$

The optical depth of a medium is a measure of mass of absorbing species on the photon path in the considered band. The depth and width of the individual water vapour absorption lines result from pressure- and temperature dependent broadening processes. Consequently, the knowledge of the actual temperature profile and the surface pressure is necessary in order to simulate the correct atmospheric transmittance. Lindstrot et al (2012) stated, that the error of a TCWV retrieval can be significantly reduced if:

1. The surface pressure reduction due to the surface elevation is accounted for, instead of taking a standard value.
2. The surface temperature from reanalysis data is used to approximate the transmittance corresponding to the actual temperature profile by adequately mixing the pre-calculated transmittance values corresponding to the two closest standard profiles [Lindstrot and Preusker, 2012].

In Eq. (1), $L_{path}(\lambda)$ and $H(\lambda)$ account for the shortening and extension of the photon path because of single and multiple scattering on aerosols. This effect is usually only a few percent of the direct reflected solar radiation in the NIR region. As introduced in [Lindstrot et al, 2012], in the retrieval of TCWV a scattering factor f accounts for this effect. It is defined as:

$$f = T^* / T_{noscat} \quad (3)$$

where T^* is the effective atmospheric transmittance including scattering (see eq. (6.)) and T_{noscat} the atmospheric transmittance in case of no scattering. f is usually larger than one, as atmospheric scattering causes a shortening of the average photon path length and reduces the amount of TCWV, by preventing a fraction of photons from traversing the humid lower troposphere. Additionally, f is increased above dark surfaces, as most part of the photons is reflected by atmospheric scatterers and thus does not travel through the whole vertical column of water vapour. Over land surfaces, one important parameter determining f is thus the surface reflectance. Over dark water surfaces, the determination of the surface brightness is even more important. A detailed investigation concerning f is given in [Lindstrot et al, 2012].

The goal of the forward-operator is to model the TOA-Radiance L_{TOA}. It is divided into two subroutines explained hereafter.

3.2 Universal forward operator

3.2.1 Transmittance processor

This subroutine derives the atmospheric transmittance due to water vapour in the absorption band. The forward operator consists of two elements: First, the calculation of the transmittance T_{noscat} and secondly the derivation of a scattering factor f. T_{noscat} which is the pure absorption part of the simulated transmittance is derived from pre-calculated absorption coefficients using an advanced k-distribution method ([Bennartz and Fischer, 2000], [Doppler et al, 2014]). The coefficients were calculated from the HITRAN 2012 line database [Rothman et al, 2013], using the AER LBLRTM code [Clough et al, 2005] for a fixed TCWV amount (WV_0). In order to obtain the optical thickness τ of the entire band, which contains a large number of spectral lines, the quasi-monochromatic intervals are sorted with respect to their optical thickness. Afterwards they are combined to a significantly lower number of pseudo-spectral intervals. The optical depths in each pseudo-spectral interval i for TCWV value of WV^* are then obtained from multiplying the stored coefficients accordingly:

$$\tau_i^* = \tau_i \frac{WV^*}{WV_0} \tag{4}$$

This is done for every vertical layer j of the preconditioned TCWV-profile. Subsequently, for every pseudo-spectral interval the transmittance is derived from the sum of the optical depth for all layers along the line of sight following Eq. (2). The total transmittance is the sum over all pseudo spectral intervals multiplied with the associated weights w_i accordingly:

$$T = \sum_{i=1}^{\#intervals} w_i * exp\left(-\sum_{j=1}^{\#layers} \tau_{ij} * amf\right) \tag{5}$$

The optical depth values τ_{ij} and the corresponding weights w_i are stored in lookup tables on 27 different pressure levels for 6 standard profiles [McClatchey et al, 1972]. These model atmospheres have been widely used in the atmospheric research community and provide standard vertical profiles of pressure, temperature, and water vapour. The transmittance is calculated for the four look-up table grid points closest to the actual surface pressure and temperature of the considered scene, hereby assuming that the surface temperature is highly correlated with the actual vertical temperature profile. The actual surface pressure is derived from converting land elevation to pressure, using the GTOPO30 digital elevation model (US Geological Survey, 1996), while the surface temperature is extracted from NWP reanalysis data (ERA interim 2m-temperature). The final transmittance of the band is then calculated as a weighted average among these four figures, with the weights determined by the distances to the closest grid points of temperature and pressure.

In order to determine the scattering correction factor f radiative transfer simulations were performed to obtain the total atmospheric transmittance (T^*) in the water vapour absorption band including scattering on air molecules and aerosol particles. T^* is defined as:

$$T^* = \frac{L_{sim}}{L_{sim}^0} \tag{6}$$

where L_{sim} is the total TOA-radiance with and L^0_{sim} is the TOA-radiance presuming a TCWV value of 0 mm.

The simulations where performed using the Matrix Operator Model (MOMO, [Fell and Fischer, 2001]; [Hollstein and Fischer, 2012]; [Doppler et al, 2014]). The radiances were calculated for different solar zenith angles (SZA), viewing zenith angles (VZA), relative azimuth angles (RAA), AOTs, surface reflectances and TCWV values and stored in LUTs.

For the water surfaces, radiative transfer simulations were performed for a dark ocean surface ($\alpha(\lambda)$=0). The surface reflectance of the ocean depends amongst others, such as on wavelength, viewing geometry, salinity and temperature on the wind-speed. Consequently, the surface

reflectance can be simulated using the wind speed for parameterizing the sea surface roughness ([Cox and Munck, 1954], [Koepke, 1985]).

The US-Standard temperature and water vapour profile was preconditioned here. The scattering properties of the aerosols were calculated using a Mie code based on [Wiscombe, 1980]. For the simulations an aerosol layer of 1500 m height with an exponential decrease of the volume-mixing ratio to the ground and continental mixture was assumed [Hess et al., 1998].

3.2.2 Surface reflectance processor

3.2.2.1 Land surfaces

This algorithm retrieves the surface reflectance in the absorption band in two steps. First, the surface reflectance in the two neighbouring window bands is obtained. Afterwards, these are either inter- or extrapolated onto the absorption band, that requires at least two window bands.

In order to obtain the surface radiance in a window band the measured radiance is first corrected for the small influence of water vapour and for the influence of aerosol scattering. The radiance corrected for water vapour L_{corr} is calculated by dividing the measured radiance L_{win} by the transmittance due to water vapour T_{noscat}^{win} in the window band:

$$L_{corr} = \frac{L^{win}}{T_{noscat}^{win}} \quad (7)$$

The determination of the surface reflectance is achieved by a LUT-approach. For that, RTSs were performed for different SZAs, VZA, RAAs, AOTs, and radiances presuming:

1. an aerosol layer with continental mixture [Hess et al., 1998] and increasing density from 1500m to the bottom
2. a standard temperature profile (U.S. Standard)
3. no water vapour in the atmosphere.

Assuming that the surface reflectance changes linearly in the considered wavelength range for the majority of surface types, the surface reflectance in the absorption band(s) is determined by linear inter- or extrapolation from the window bands, depending on the position of the bands.

3.2.2.2 Water surfaces

The determination of the water surface reflectance is as described for land surfaces by a LUT-approach. For that, RTSs were performed for different SZAs, VZA, RAAs, AOTs, wind speeds and radiances presuming:

1. An aerosol layer with maritime aerosol [Hess et al., 1998] and increasing density from 1500m to the bottom;
2. A standard temperature profile (U.S. Standard);
3. No water vapour in the atmosphere;
4. The true ocean surface reflectance is approximated from the wind speed and the observing geometry ([Cox and Munck, 1954], [Koepke, 1984]).

The surface winds are extracted from NWP reanalysis data (ERA interim u,v-wind; http://www.ecmwf.int/research/era/do/get/era-interim)

3.3 Retrieval scheme

This retrieval derives TCWV values with the help of an inverse modelling scheme. Deviations between modelled and measured radiances in the absorption bands are iteratively reduced by changing the

water vapour amount. In order to include information from all absorption bands and to account for the measurement error in the inversion scheme, the inversion technique presented in Sect. 3.3.1 is used. The uncertainty estimate is derived after the last retrieval step, by taking into account all error influences (Sect. 3.3.2). The individual retrieval steps are described in the following sections.

3.3.1 Inversion technique

Only one state vector variable has to be found in the iterative optimization routine: The total column water vapour. Starting with the first guess, TCWV is adapted by minimizing the differences between simulated and measured radiances. The TCWV value for the next iteration step is derived by the following scheme after [Rodgers, 2000]:

$$G = (K^T S_e^{-1} K)^{-1} (K^T S_e^{-1}) \quad (8)$$

$$x_{i+1} = x_i + (G(y - F_i)) \quad (9)$$

where K is the Jacobian matrix that contains the partial derivatives of the radiance to the TCWV value in each band, S_e the measurement error covariance matrix which contains the measured radiance scaled with the signal to noise ratio (SNR) for each band. y contains the measured and F_i the modelled radiances. The first guess of TCWV f_g is obtained from a simple regression, relating TCWV to a third order polynomial of $ln(T_{noscat})$ for single absorption band (e.g. band 17 of MODIS):

$$f_g = 2/\mu * c_1 - ln(T_{17}) * c_2 + (ln(T_{17}))^2 * c_3 \quad (10)$$

where μ is again the air mass. The regression coefficients (c_i) were determined using the absorption forward operator (example for MODIS band 17 is given in Table 3).

Table 3: Regression coefficients between transmittance and TCWV for the determination of the first guess from the transmittance of MODIS band 17.

	C_1	C_2	C_3
coefficients	0.0746699	-1.15649	19.9892

3.3.2 Uncertainty estimate

After the iteration procedure the retrieval uncertainty is calculated, taking into account the following sources of uncertainty:

- residual model error
- instrument uncertainty (SNR)
- uncertainty of the aerosol optical depth
- uncertainty due to the missing information of the aerosol type and scale height
- uncertainty of the surface pressure and -temperature
- uncertainty due to the missing information about the true temperature profile
- uncertainty due to the estimation of the surface reflectance and spectral slope

For the error quantification, these model parameter uncertainties assembled in the error covariance matrix S_b are propagated into the measurement space using the standard error propagation and added to the measurement error covariance matrix S_e:

$$S_y = S_e + K_b^T S_b K_b \quad (11)$$

where K_b is the parameter Jacobian. The resulting error covariance matrix S_y is then propagated into the state vector space using the Jacobian K that is the partial derivative of the modelled radiance

with respect to the TCWV for each band. The resulting error covariance matrix S is a direct measure of uncertainty in TCWV space [Rodgers, 2000]:

$$\hat{S}^{-1} = K^T S_y^{-1} K \quad (12)$$

In the following, it is described, how the individual error sources are estimated. As outlined before, the scattering factor f is affected most by the surface reflectance, aerosol height and -optical thickness. For each of these parameters a perturbed f^* is calculated from the look-up tables, by perturbing the input accordingly. There is no information available about the aerosol scale height and the type (size distribution, absorption and scattering properties). Consequently, a f^* was calculated presuming an aerosol layer at 6000 m with a thickness of 500 m. Additionally, a f^* was calculated from simulations supposing another aerosol model. These f^* were used to derive perturbed TOA-radiances L^*_{TOA}. Finally, the difference $(\Delta L)^2 = (L_{TOA} - L^*_{TOA})^2$ is added to the measurement error variance S_e.

The error due to differences between the simulation- and the real temperature- (and humidity-) profile was evaluated by comparing the atmospheric transmittances derived from a real example radiosonde profile to transmittance using the standard profiles. This effect introduces an error to the pure absorption transmittance of around 2 % (depending on the band). To estimate the uncertainty due to the surface background information, the surface temperature was shifted 5 K and the surface pressure was perturbed by 20 hPa and subsequently committed to the transmittance forward operator. Again, $(\Delta L)^2$ is calculated and added to S_e.

The uncertainty of the spectral dependency of the surface reflectance is parameterized with the Normalized Differenced Vegetation Index (NDVI): $NDVI = (\rho_{865nm} - \rho_{670nm})/(\rho_{865nm} + \rho_{670nm})$. For each absorption band and for a set of *NDVI* values an error was calculated beforehand from the difference between true surface reflectance and the interpolated value for large number of surface reflectance spectra (for further details see [Lindstrot et al, 2012]).

The uncertainties of the surface reflectance range from 0.5 to 1.2 %. Similar to the approach pictured above, a perturbed TOA radiance is calculated and the resulting deviation is contributed to S_e. Finally the residual model error, that is the difference between measurement and modelled radiance from the last iteration step is added to the measurement covariance matrix that consists of the sensor noise.

4 Input Output Data

This section defines the input data, required for the processing of MERIS, OLCI and MODIS data as well as the output of the water vapor processor.

The TCWV processor is using normalised radiances. The observation geometry is expressed in viewing zenith angle, Sun zenith angle and azimuth difference angle, which are all given in the L1b product-files (see Table 4a).

Table 4a: Satellite measurements taken from the Level 1b instrument data files.

Quantity	Unit	Valid range	Source	Comment
Normalized radiance	1/sr	0 -1	L1b	Depending on instrument different bands serve as absorption and as window bands (see Section 1.3)
Viewing zenith angle	deg	0-60	L1b	
Sun zenith angle	deg	0-75	L1b	
Azimuth difference angle	deg	0-180	L1b	

The auxiliary data used in the TCWV processor are taken for MERIS and OLCI from ESA's meteorology data-files provided by ECWMF, and additional accessible data on aerosols, i.e. from ESA/NASA

archive. For MODIS the ERA-interim data are used (see Table 4b).

Table 4b: Auxiliary data used in the TCWV processor and it's valid range.

Quantity	Unit	Valid range	Source	Comment
Surface pressure	hPa	1050-200	QNH from ECMWF, adapted to actual surface height	GFS is also possible
Surface temperature	K	260-330	ECMWF	
Aerosol optical thickness	1	0-1.0	Ideally GRASP, or MODIS 8-day average	If no available, climatology can be used (0.1)
Aerosol optical thickness uncertainty	1		Taken from GRASP or MODIS, resp.	
Wind-speed	m/s	2-15	ECMWF	Only over water

The output of the TCWV processor is the total column water vapour and it's uncertainty in kg/m^2. For further analysis of the convergence of the inversion process, the estimated transmission and the number of required iterations are given (see Table 5).

Table 5: Output of the TCWV algorithm after applying to the Level 1b instrument data files; TCWV and it's estimated uncertainty, convergence as a logical expression, intermediate results to check the inversion process.

Quantity	Unit	Valid range	Source	Comment
TCWV	Kg/m2	0-75		
TCWW uncertainty	Kg/m2	0-60		
Convergence	logical			
Intermediate results, i.e. first guess, transmission, number of iterations				Can be used for debugging purpose

The processor is divided into two main units. One unit is responsible for all input-output operations; the other unit is retrieving the TCWV for a single pixel. The communication between both units is performed using files, pipes or streams in JSON. This allows the easy exchange of modules for testing and developing. The operational IO part is BEAM. The water vapour part is written in python and FORTRAN.

4.1 Input structure

The following lines give an example for the JSON input for the processor configured for MODIS (the comment behind the hash signs are not part of the JSON)

```
{'tmp':303.                  # surface temperature (or 2m) in [K]
,'prs':1003.                 # surface pressure  [hPa]
,'suz':9.7968997955322270    # sun zenith  [deg]
,'vie':46.12860107421875     # view zenith [deg]
,'azi':18.                   # azimuth difference = view_azi-sun_azi (0,...180) [deg]
,'aot': {'2':0.1             # aot at wavelength of band 2
       , '5':0.08            # aot at wavelength of band 5
       , '17':0.1            # aot at wavelength of band 17
       , '18':0.1            # aot at wavelength of band 18
       , '19':0.1            # aot at wavelength of band 19
        }
```

```
    ,'sig_aot': {'2':0.1          # uncertainty of aot at wavelength of band 2
           , '5':0.1              # uncertainty of aot at wavelength of band 5
           , '17':0.1             # uncertainty of aot at wavelength of band 17
           , '18':0.1             # uncertainty of aot at wavelength of band 18
           , '19':0.1             # uncertainty of aot at wavelength of band 19
            }
    ,'rtoa':{'2':  0.0636619783227144       # normalized radiance in band 2
           , '5':  0.06525352778078226     # normalized radiance in band 5
           , '17': 0.050292962874944384    # normalized radiance in band 17
           , '18': 0.019098593496814323     # normalized radiance in band 18
           , '19': 0.029921129811675773    # normalized radiance in band 19
            }
       }
```

4.2 Output structure

The following lines show a corresponding example output. Most lines are only useful for debugging. Relevant are the TCWV fields.

```
{'alb': {'17': 0.20744058708043236,
         '18': 0.20803469858273346,
         '19': 0.2080450532480437,
         '2': 0.20653781139830463,
         '5': 0.21382843735086557},
 'amf': 2.4577125799685628,
 'aot': {'17': 0.1, '18': 0.1, '19': 0.1, '2': 0.1, '5': 0.08},
 'azi': 18.0,
 'convergence': true,
 'fgu': 13.325100325715178,    #first guess TCWV in kg/m2
 'niter': 3,
 'prs': 1003.0,
 'rtoa': {'17': 0.050292962874944384,
          '18': 0.019098593496814323,
          '19': 0.029921129811675773,
          '2': 0.0636619783227144,
          '5': 0.06525352778078226},
 'rtoa_0': {'17': 0.06492165866278476,
            '18': 0.06501949555510961,
            '19': 0.06502120073716902,
            '2': 0.06477299167542006,
            '5': 0.06597359490147904},
 'sig_aot': {'17': 0.1, '18': 0.1, '19': 0.1, '2': 0.1, '5': 0.1},
 'sig_tcwv': 0.7624883523001241, #uncertainty TCWV in kg/m2
 'suz': 9.796899795532227,
 'tcwv': 15.249767046002482,  #retrieved TCWV in kg/m2
 'tmp': 303.0,
 'trans_fg': {'17': 0.8018521635828549, # gaseous transmission for retrieved TCWV & geometry
              '18': 0.31104987302486253, # gaseous transmission for retrieved TCWV & geometry
              '19': 0.47906689882847997, # gaseous transmission for retrieved TCWV & geometry
              '2': 0.9828475831674877, # gaseous transmission for retrieved TCWV & geometry
              '5': 0.9890855254776993}, # gaseous transmission for retrieved TCWV & geometry
 'vie': 46.12860107421875}
```

5 Assumptions and limitations

Generally, the quality of the TCWV retrieval algorithm strongly depends on the reliability of the cloud mask. For example MERIS does not provide measurements in the thermal infrared, the screening of

optically thin cirrus clouds is difficult. A dry bias is to be expected, where the cloud detection fails to detect cirrus clouds. For other detector such as MODIS cloud-mask-products are reliable and available.

Additionally, the SNR increases in the NIR for low surfaces reflectances especially over the ocean. Consequently, the uncertainty over water surfaces is increased, particularly to the edge of the swath that is not influenced by sun glint.

6 Conclusions

A new retrieval method has been defined and developed to estimate TCWV from satellite measurements, using the $\rho\sigma\tau$-H_2O absorption band. The 1D-Var algorithm is based on a fast forward operator, which contains three main sub-procedures for: (1) surface reflectance, (2) transmittance due to atmospheric water vapour, and (3) shortening of the photon path due to atmospheric scattering. A realistic uncertainty estimate is given on a pixel-by-pixel basis where the uncertainties of measurement and forward model are considered respectively.

It is intended to use transmission correction not only to increase the accuracy but also to homogenize time series of TCWV over land from different satellites such as MERIS, MODIS and OLCI. However, due to additional channels within the $\rho\sigma\tau$-H_2O absorption band of MODIS and OLCI with respect to MERIS, the retrieval accuracy increases, especially above darker surfaces, such as water [Diedrich et al, 2012].

Validation results for the adaption to MERIS measurements over land surfaces can be found in Lindstrot et al (2012) and for MODIS in Diedrich et al (2014).

7 References

Albert, P., R. Bennartz, and J. Fischer, 2001: Remote Sensing of Atmospheric Water Vapor from Backscattered Sunlight in Cloudy Atmospheres. Journal of Atmospheric and Oceanic Technology, 18:865.

Albert, P., R. Bennartz, R. Preusker, R. Leinweber, and J. Fischer, 2005: Remote Sensing of Atmospheric Water Vapor Using the Moderate Resolution Imaging Spectroradiometer. Journal of Atmospheric and Oceanic Technology, 22:309.

Bartsch, B., S. Bakan, and J. Fischer, 1996: Passive remote sensing of the atmospheric water vapour content above land surfaces. Advances in Space Research, 18:25–28.

Bennartz, R. and J. Fischer, 2000: A modified k-distribution approach applied to narrow band water vapour and oxygen absorption estimates in the near infrared. Journal of Quantitative Spectroscopy & Radiative Transfer, 66:539–553.

Clough, S. A. , M. W. Shephard, E. J. Mlawer, J. S. Delamere, M. J. Iacono, K. Cady-Pereira, S. Boukabara, and P. D. Brown, 2005: Atmospheric radiative transfer modeling: a summary of the AER codes. Journal of Quantitative Spectroscopy & Radiative Transfer, 91:233–244.

Cox, C. and W. Munk, 1954: Measurement of the roughness of the sea surface from photographs of the sun's glitter. Journal of the Optical Society of America (1917- 1983), 44:838.

Diedrich, H., R. Preusker, R. Lindstrot, and J. Fischer, 2015: Retrieval of daytime total columnar water vapour from modis measurements over land surfaces. Atmospheric Measurement Techniques, 8:823-836.

Doppler, L., C. Carbajal-Henken, J. Pelon, F. Ravetta, and J. Fischer, 2014: Extension of radiative transfer code MOMO, matrix-operator model to the thermal infrared - Clear air validation by comparison to RTTOV and application to CALIPSO IIR, 144:49–67.

Fell, F. and J. Fischer, 2001: Numerical simulation of the light field in the atmosphereocean system using the matrix-operator method. Journal of Quantitative Spectroscopy & Radiative Transfer, 69: 351–388.

Fischer, J. 1988: High Resolution Spectroscopy for Remote Sensing of Physical Cloud Properties and Water Vapour. In: Current Problems in Atmospheric Radiation, Ed. Lenoble and Geleyn, Deepak Publishing, 151-156.

Fischer, J. and H. Grassl. Radiative transfer in an atmosphere-ocean system: an azimuthally dependent matrix-operator approach. Applied Optics, 23:1032–1039, Apr. 1984.

Gao, B.-C. and A. F. H. Goetz, 1990: Column atmospheric water vapor and vegetationliquid water retrievals from Airborne Imaging Spectrometer data. Journal of Geophysic Research, 95: 3549–3564.

Gao, B.-C., A. F. H. Goetz, E. R. Westwater, J. E. Conel, and R. O. Green, 1993: Possible Near-IR Channels for Remote Sensing Precipitable Water Vapor from Geostationary Satellite Platforms. Journal of Applied Meteorology, 32: 1791–1801.

Hansen, J. E. and L. D. Travis. Light scattering in planetary atmospheres. , 16:527–610, Oct. 1974.

Held, I. and Soden, B., 2000: Water vapor feedback and global warming, Annu. Rev. Energy Environ., 25: 441-475.

Hess, M., P. Koepke, and I. Schult, 1998: Optical Properties of Aerosols and Clouds: The Software Package OPAC. Bulletin of the American Meteorological Society, 79: 831–844.

Hollstein, A. and J. Fischer, 2012: Radiative transfer solutions for coupled atmosphere ocean systems using the matrix operator technique. Journal of Quantitative Spectroscopy & Radiative Transfer, 113: 536–548.

Koepke, P., 1985: The reflectance factors of a rough ocean with foam - comment on 'Remote sensing of the sea state using the 08-11 _m spectral band' by L. Wald and J. M. Monget. International Journal of Remote Sensing, 6: 787–797.

Lindstrot, R. and R. Preusker, 2012: On the efficient treatment of temperature profiles for the estimation of atmospheric transmittance under scattering conditions. Atmospheric Measurement Techniques, 5: 2525–2535.

Lindstrot, R., R. Preusker, H. Diedrich, L. Doppler, R. Bennartz, and J. Fischer, 2012: 1D-Var retrieval of daytime total columnar water vapour from MERIS measurements. Atmospheric Measurement Techniques, 5: 631–646.

McClatchey, R., R. Fenn, J. Selby, F. Volz, and J. Garing, 1972: Optical properties of the atmosphere (3rd ed.). Technical report, Air Force Cambridge Research Laboratories.

Rodgers, C., 2000: Inverse Methods for Atmospheric Sounding: Theory and Practice. World Scientific Pub Co.

Rothman, L.S, I.E. Gordon, Y. Babikov, A. Barbe, D.C. Benner, P.F. Bernath, et al., 2013: The HITRAN2012 molecular spectroscopic database. JQSRT, Volume 130, Pages 4-50.

Trenberth, K.E., and D.P. Stepaniak, 2003a: Co-variability of components of poleward atmospheric energy transports on seasonal and interannual timescales. J. Clim., 16: 3690–3704.

Trenberth, K.E., and D.P. Stepaniak, 2003b: Seamless poleward atmospheric energy transports and

implications for the Hadley circulation. J. Clim. 16: 3705–3721.

Wiscombe, W.J., 1980: Improved Mie scattering algorithms. Applied Optics 19: 1505– 1509.